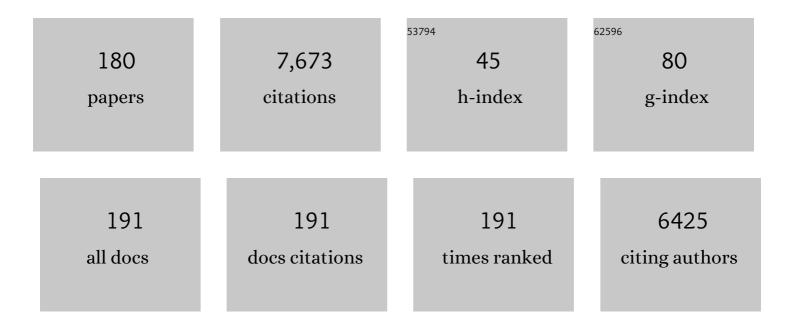
Zhenhong Li

List of Publications by Year in descending order

Source: https://exaly.com/author-pdf/9578645/publications.pdf Version: 2024-02-01



| # | Article | IF | CITATIONS |
|----|---|------|-----------|
| 1 | Unmanned Aerial Vehicle Remote Sensing for Field-Based Crop Phenotyping: Current Status and Perspectives. Frontiers in Plant Science, 2017, 8, 1111. | 3.6 | 448 |
| 2 | Random Forest and Rotation Forest for fully polarized SAR image classification using polarimetric and spatial features. ISPRS Journal of Photogrammetry and Remote Sensing, 2015, 105, 38-53. | 11.1 | 357 |
| 3 | Generic Atmospheric Correction Model for Interferometric Synthetic Aperture Radar Observations. Journal of Geophysical Research: Solid Earth, 2018, 123, 9202-9222. | 3.4 | 326 |
| 4 | Partial rupture of a locked patch of the Sumatra megathrust during the 2007 earthquake sequence. Nature, 2008, 456, 631-635. | 27.8 | 308 |
| 5 | Interferometric synthetic aperture radar atmospheric correction using a GPS-based iterative tropospheric decomposition model. Remote Sensing of Environment, 2018, 204, 109-121. | 11.0 | 237 |
| 6 | Improving InSAR geodesy using Global Atmospheric Models. Journal of Geophysical Research: Solid Earth, 2014, 119, 2324-2341. | 3.4 | 220 |
| 7 | Comparison of precipitable water vapor derived from radiosonde, GPS, and Moderate-Resolution Imaging Spectroradiometer measurements. Journal of Geophysical Research, 2003, 108, . | 3.3 | 209 |
| 8 | Generation of realâ€time mode highâ€resolution water vapor fields from GPS observations. Journal of Geophysical Research D: Atmospheres, 2017, 122, 2008-2025. | 3.3 | 182 |
| 9 | Interferometric synthetic aperture radar (InSAR) atmospheric correction: GPS, Moderate Resolution Imaging Spectroradiometer (MODIS), and InSAR integration. Journal of Geophysical Research, 2005, 110, | 3.3 | 146 |
| 10 | Extension on the Tibetan plateau: recent normal faulting measured by InSAR and body wave seismology. Geophysical Journal International, 2010, 183, 503-535. | 2.4 | 146 |
| 11 | Monitoring activity at the Daguangbao mega-landslide (China) using Sentinel-1 TOPS time series interferometry. Remote Sensing of Environment, 2016, 186, 501-513. | 11.0 | 145 |
| 12 | Imaging Land Subsidence Induced by Groundwater Extraction in Beijing (China) Using Satellite Radar Interferometry. Remote Sensing, 2016, 8, 468. | 4.0 | 142 |
| 13 | Evaluating sub-pixel offset techniques as an alternative to D-InSAR for monitoring episodic landslide movements in vegetated terrain. Remote Sensing of Environment, 2014, 147, 133-144. | 11.0 | 134 |
| 14 | Interferometric synthetic aperture radar atmospheric correction: GPS topography-dependent turbulence model. Journal of Geophysical Research, 2006, 111, n/a-n/a. | 3.3 | 120 |
| 15 | Advanced InSAR atmospheric correction: MERIS/MODIS combination and stacked water vapour models. International Journal of Remote Sensing, 2009, 30, 3343-3363. | 2.9 | 119 |
| 16 | Highâ€Resolution Surface Velocities and Strain for Anatolia From Sentinelâ€1 InSAR and GNSS Data. Geophysical Research Letters, 2020, 47, e2020GL087376. | 4.0 | 108 |
| 17 | Using advanced InSAR time series techniques to monitor landslide movements in Badong of the Three Gorges region, China. International Journal of Applied Earth Observation and Geoinformation, 2013, 21, 253-264. | 2.8 | 105 |
| 18 | Slip in the 2010–2011 Canterbury earthquakes, New Zealand. Journal of Geophysical Research, 2012, 117, . | 3.3 | 103 |

| # | Article | IF | CITATIONS |
|----|--|-----|-----------|
| 19 | Dual control of fault intersections on stop-start rupture in the 2016 Central Italy seismic sequence. Earth and Planetary Science Letters, 2018, 500, 1-14. | 4.4 | 100 |
| 20 | Using wavelet tools to analyse seasonal variations from InSAR time-series data: a case study of the Huangtupo landslide. Landslides, 2016, 13, 437-450. | 5.4 | 99 |
| 21 | Kinematic fault slip evolution source models of the 2008 M7.9 Wenchuan earthquake in China from SAR interferometry, GPS and teleseismic analysis and implications for Longmen Shan tectonics. Geophysical Journal International, 2013, 194, 1138-1166. | 2.4 | 97 |
| 22 | Entering the Era of Earth Observation-Based Landslide Warning Systems: A Novel and Exciting Framework. IEEE Geoscience and Remote Sensing Magazine, 2020, 8, 136-153. | 9.6 | 90 |
| 23 | Integration of InSAR Time-Series Analysis and Water-Vapor Correction for Mapping Postseismic Motion After the 2003 Bam (Iran) Earthquake. IEEE Transactions on Geoscience and Remote Sensing, 2009, 47, 3220-3230. | 6.3 | 88 |
| 24 | Integration of Sentinel-1 and ALOS/PALSAR-2 SAR datasets for mapping active landslides along the Jinsha River corridor, China. Engineering Geology, 2021, 284, 106033. | 6.3 | 88 |
| 25 | The 2010 <i>M</i> _{<i>W</i>} 6.8 Yushu (Qinghai, China) earthquake: Constraints provided by InSAR and body wave seismology. Journal of Geophysical Research, 2011, 116, . | 3.3 | 84 |
| 26 | Assessment of the potential of MERIS nearâ€infrared water vapour products to correct ASAR interferometric measurements. International Journal of Remote Sensing, 2006, 27, 349-365. | 2.9 | 83 |
| 27 | Evaluation of ASTER GDEM using GPS benchmarks and SRTM in China. International Journal of Remote Sensing, 2013, 34, 1744-1771. | 2.9 | 82 |
| 28 | Interferometric synthetic aperture radar atmospheric correction: Medium Resolution Imaging Spectrometer and Advanced Synthetic Aperture Radar integration. Geophysical Research Letters, 2006, 33, . | 4.0 | 78 |
| 29 | Application of DInSAR-GPS Optimization for Derivation of Fine-Scale Surface Motion Maps of Southern California. IEEE Transactions on Geoscience and Remote Sensing, 2007, 45, 512-521. | 6.3 | 76 |
| 30 | The 2011 MW 6.8 Burma earthquake: fault constraints provided by multiple SAR techniques. Geophysical Journal International, 2013, 195, 650-660. | 2.4 | 71 |
| 31 | Multi-GNSS precise point positioning for precision agriculture. Precision Agriculture, 2018, 19, 895-911. | 6.0 | 69 |
| 32 | Postseismic motion after the 2001 M _W 7.8 Kokoxili earthquake in Tibet observed by InSAR time series. Journal of Geophysical Research, 2012, 117, . | 3.3 | 67 |
| 33 | Distribution and characteristics of loess landslides triggered by the 1920 Haiyuan Earthquake, Northwest of China. Geomorphology, 2018, 314, 1-12. | 2.6 | 67 |
| 34 | Potassium and Obesity/Metabolic Syndrome: A Systematic Review and Meta-Analysis of the Epidemiological Evidence. Nutrients, 2016, 8, 183. | 4.1 | 64 |
| 35 | Extracting Vertical Displacement Rates in Shanghai (China) with Multi-Platform SAR Images. Remote Sensing, 2015, 7, 9542-9562. | 4.0 | 62 |
| 36 | lmaging ionospheric inhomogeneities using spaceborne synthetic aperture radar. Journal of Geophysical Research, 2011, 116, n/a-n/a. | 3.3 | 57 |

| # | Article | IF | CITATIONS |
|----|--|------|-----------|
| 37 | Rapid strain accumulation on the Ashkabad fault (Turkmenistan) from atmosphereâ€corrected InSAR. Journal of Geophysical Research: Solid Earth, 2013, 118, 3674-3690. | 3.4 | 57 |
| 38 | Improved Estimation of Winter Wheat Aboveground Biomass Using Multiscale Textures Extracted from UAV-Based Digital Images and Hyperspectral Feature Analysis. Remote Sensing, 2021, 13, 581. | 4.0 | 56 |
| 39 | Multi-LUTs method for canopy nitrogen density estimation in winter wheat by field and UAV hyperspectral. Computers and Electronics in Agriculture, 2019, 162, 174-182. | 7.7 | 55 |
| 40 | Spatiotemporal characteristics of the Huangtupo landslide in the Three Gorges region (China) constrained by radar interferometry. Geophysical Journal International, 2014, 197, 213-232. | 2.4 | 54 |
| 41 | Land subsidence in Beijing and its relationship with geological faults revealed by Sentinel-1 InSAR observations. International Journal of Applied Earth Observation and Geoinformation, 2019, 82, 101886. | 2.8 | 53 |
| 42 | A hybrid modelling approach to understanding adoption of precision agriculture technologies in Chinese cropping systems. Computers and Electronics in Agriculture, 2020, 172, 105305. | 7.7 | 52 |
| 43 | Three-dimensional time-varying large surface displacements in coal exploiting areas revealed through integration of SAR pixel offset measurements and mining subsidence model. Remote Sensing of Environment, 2020, 240, 111663. | 11.0 | 52 |
| 44 | Contemporary uplift of the Sierra Nevada, western United States, from GPS and InSAR measurements. Geology, 2012, 40, 667-670. | 4.4 | 51 |
| 45 | Land subsidence prediction in Beijing based on PS-InSAR technique and improved Grey-Markov model. GIScience and Remote Sensing, 2017, 54, 797-818. | 5.9 | 51 |
| 46 | Estimating genetic parameters of DSSAT-CERES model with the GLUE method for winter wheat (Triticum aestivum L.) production. Computers and Electronics in Agriculture, 2018, 154, 213-221. | 7.7 | 50 |
| 47 | Deformation Monitoring of Reservoir Dams Using GNSS: An Application to South-to-North Water Diversion Project, China. IEEE Access, 2019, 7, 54981-54992. | 4.2 | 48 |
| 48 | Earth Observations for Geohazards: Present and Future Challenges. Remote Sensing, 2017, 9, 194. | 4.0 | 46 |
| 49 | Winter Wheat Nitrogen Status Estimation Using UAV-Based RGB Imagery and Gaussian Processes Regression. Remote Sensing, 2020, 12, 3778. | 4.0 | 46 |
| 50 | Source characteristics of the 2015 MW 7.8 Gorkha (Nepal) earthquake and its MW 7.2 aftershock from space geodesy. Tectonophysics, 2017, 712-713, 747-758. | 2.2 | 43 |
| 51 | Triggered afterslip on the southern Hikurangi subduction interface following the 2016 KaikÅura earthquake from InSAR time series with atmospheric corrections. Remote Sensing of Environment, 2020, 251, 112097. | 11.0 | 41 |
| 52 | Comparison and transferability of thermal, temporal and phenological-based in-season predictions of above-ground biomass in wheat crops from proximal crop reflectance data. Remote Sensing of Environment, 2022, 273, 112967. | 11.0 | 41 |
| 53 | Sensitivity of Coulomb stress change to the parameters of the Coulomb failure model: A case study using the 2008 <i>M_w</i> 7.9 Wenchuan earthquake. Journal of Geophysical Research: Solid Earth, 2014, 119, 3371-3392. | 3.4 | 40 |
| 54 | A hierarchical interannual wheat yield and grain protein prediction model using spectral vegetative indices and meteorological data. Field Crops Research, 2020, 248, 107711. | 5.1 | 40 |

| # | Article | IF | CITATIONS |
|----|--|-----|-----------|
| 55 | Kinematic model of crustal deformation of Fenwei basin, China based on GPS observations. Journal of Geodynamics, 2014, 75, 1-8. | 1.6 | 39 |
| 56 | Drought Evaluation with CMORPH Satellite Precipitation Data in the Yellow River Basin by Using Gridded Standardized Precipitation Evapotranspiration Index. Remote Sensing, 2019, 11, 485. | 4.0 | 39 |
| 57 | Applying the Coulomb failure function with an optimally oriented plane to the 2008 Mw 7.9 Wenchuan earthquake triggering. Tectonophysics, 2010, 491, 119-126. | 2.2 | 38 |
| 58 | Remote Sensing of Leaf and Canopy Nitrogen Status in Winter Wheat (Triticum aestivum L.) Based on N-PROSAIL Model. Remote Sensing, 2018, 10, 1463. | 4.0 | 38 |
| 59 | Capability of Remotely Sensed Drought Indices for Representing the Spatio–Temporal Variations of the Meteorological Droughts in the Yellow River Basin. Remote Sensing, 2018, 10, 1834. | 4.0 | 37 |
| 60 | Monitoring Highway Stability in Permafrost Regions with X-band Temporary Scatterers Stacking InSAR. Sensors, 2018, 18, 1876. | 3.8 | 37 |
| 61 | Post-disaster assessment of 2017 catastrophic Xinmo landslide (China) by spaceborne SAR interferometry. Landslides, 2019, 16, 1189-1199. | 5.4 | 36 |
| 62 | Deformation of the Baige Landslide, Tibet, China, Revealed Through the Integration of Crossâ€Platform ALOS/PALSARâ€1 and ALOS/PALSARâ€2 SAR Observations. Geophysical Research Letters, 2020, 47, e2019GL086142. | 4.0 | 36 |
| 63 | Anatomy of Subsidence in Tianjin from Time Series InSAR. Remote Sensing, 2016, 8, 266. | 4.0 | 33 |
| 64 | Patterns and mechanisms of coseismic and postseismic slips of the 2011 M W 7.1 Van (Turkey) earthquake revealed by multi-platform synthetic aperture radar interferometry. Tectonophysics, 2014, 632, 188-198. | 2.2 | 32 |
| 65 | Short-term effects of atmospheric particulate matter on myocardial infarction: a cumulative meta-analysis. Environmental Science and Pollution Research, 2016, 23, 6139-6148. | 5.3 | 32 |
| 66 | GNSS tropospheric gradients with high temporal resolution and their effect on precise positioning. Journal of Geophysical Research D: Atmospheres, 2016, 121, 912-930. | 3.3 | 30 |
| 67 | Crop Water Content of Winter Wheat Revealed with Sentinel-1 and Sentinel-2 Imagery. Sensors, 2019, 19, 4013. | 3.8 | 30 |
| 68 | Precision agriculture technology adoption: a qualitative study of small-scale commercial "family farms―located in the North China Plain. Precision Agriculture, 2022, 23, 319-351. | 6.0 | 30 |
| 69 | Using CYGNSS Data to Map Flood Inundation during the 2021 Extreme Precipitation in Henan Province, China. Remote Sensing, 2021, 13, 5181. | 4.0 | 30 |
| 70 | Land Subsidence over Oilfields in the Yellow River Delta. Remote Sensing, 2015, 7, 1540-1564. | 4.0 | 29 |
| 71 | Landslide Detection in the Linzhi–Ya'an Section along the Sichuan–Tibet Railway Based on InSAR and Hot Spot Analysis Methods. Remote Sensing, 2021, 13, 3566. | 4.0 | 29 |
| 72 | Quantifying the influence of long-term overexploitation on deep groundwater resources across Cangzhou in the North China Plain using InSAR measurements. Journal of Hydrology, 2022, 605, 127368. | 5.4 | 28 |

| # | Article | IF | CITATIONS |
|----|--|------|-----------|
| 73 | Automatic Extraction of Water and Shadow from SAR Images Based on a Multi-Resolution Dense Encoder and Decoder Network. Sensors, 2019, 19, 3576. | 3.8 | 27 |
| 74 | Resolving Surface Displacements in Shenzhen of China from Time Series InSAR. Remote Sensing, 2018, 10, 1162. | 4.0 | 26 |
| 75 | Progress of hyperspectral data processing and modelling for cereal crop nitrogen monitoring. Computers and Electronics in Agriculture, 2020, 172, 105321. | 7.7 | 26 |
| 76 | Spatiotemporal Changes of Coastline over the Yellow River Delta in the Previous 40 Years with Optical and SAR Remote Sensing. Remote Sensing, 2021, 13, 1940. | 4.0 | 26 |
| 77 | Measurement of subsidence in the Yangbajing geothermal fields, Tibet, from TerraSAR-X InSAR time series analysis. International Journal of Digital Earth, 2016, 9, 697-709. | 3.9 | 25 |
| 78 | A new approach to selecting coherent pixels for ground-based SAR deformation monitoring. ISPRS Journal of Photogrammetry and Remote Sensing, 2018, 144, 412-422. | 11.1 | 25 |
| 79 | Resolving Fine-Scale Surface Features on Polar Sea Ice: A First Assessment of UAS Photogrammetry Without Ground Control. Remote Sensing, 2019, 11, 784. | 4.0 | 25 |
| 80 | New insights into the 2020 Sardoba dam failure in Uzbekistan from Earth observation. International Journal of Applied Earth Observation and Geoinformation, 2022, 107, 102705. | 2.8 | 25 |
| 81 | The 1998 <i>M</i> _{<i>w</i>} 5.7 Zhangbeiâ€Shangyi (China) earthquake revisited: A buried thrust fault revealed with interferometric synthetic aperture radar. Geochemistry, Geophysics, Geosystems, 2008, 9, . | 2.5 | 24 |
| 82 | High interseismic coupling in the Eastern Makran (Pakistan) subduction zone. Earth and Planetary Science Letters, 2015, 420, 116-126. | 4.4 | 24 |
| 83 | Coastal Dam Inundation Assessment for the Yellow River Delta: Measurements, Analysis and Scenario. Remote Sensing, 2020, 12, 3658. | 4.0 | 24 |
| 84 | Watch Out for the Tailings Pond, a Sharp Edge Hanging over Our Heads: Lessons Learned and Perceptions from the Brumadinho Tailings Dam Failure Disaster. Remote Sensing, 2021, 13, 1775. | 4.0 | 24 |
| 85 | Reconstructing of High-Spatial-Resolution Three-Dimensional Electron Density by Ingesting SAR-Derived VTEC Into IRI Model. IEEE Geoscience and Remote Sensing Letters, 2022, 19, 1-5. | 3.1 | 24 |
| 86 | Copula-Based Drought Analysis Using Standardized Precipitation Evapotranspiration Index: A Case Study in the Yellow River Basin, China. Water (Switzerland), 2019, 11, 1298. | 2.7 | 23 |
| 87 | Global Comparisons of ERA5 and the Operational HRES Tropospheric Delay and Water Vapor Products With GPS and MODIS. Earth and Space Science, 2021, 8, e2020EA001417. | 2.6 | 22 |
| 88 | A new agricultural drought index for monitoring the water stress of winter wheat. Agricultural Water Management, 2021, 244, 106599. | 5.6 | 21 |
| 89 | Small Magnitude Co-Seismic Deformation of the 2017 Mw 6.4 Nyingchi Earthquake Revealed by InSAR Measurements with Atmospheric Correction. Remote Sensing, 2018, 10, 684. | 4.0 | 20 |
| 90 | Sequential Estimation of Dynamic Deformation Parameters for SBAS-InSAR. IEEE Geoscience and Remote Sensing Letters, 2020, 17, 1017-1021. | 3.1 | 20 |

| # | Article | IF | CITATIONS |
|-----|---|------|-----------|
| 91 | Measuring the Urban Land Surface Temperature Variations Under Zhengzhou City Expansion Using Landsat-Like Data. Remote Sensing, 2020, 12, 801. | 4.0 | 20 |
| 92 | Evaluation of the Stability of the Darbandikhan Dam after the 12 November 2017 Mw 7.3 Sarpol-e Zahab (Iran–Iraq Border) Earthquake. Remote Sensing, 2018, 10, 1426. | 4.0 | 19 |
| 93 | In-season biomass estimation of oilseed rape (Brassica napus L.) using fully polarimetric SAR imagery. Precision Agriculture, 2019, 20, 630-648. | 6.0 | 19 |
| 94 | A New Deep Learning Algorithm for SAR Scene Classification Based on Spatial Statistical Modeling and Features Re-Calibration. Sensors, 2019, 19, 2479. | 3.8 | 19 |
| 95 | UAV-Based Photogrammetry and LiDAR for the Characterization of Ice Morphology Evolution. IEEE Journal of Selected Topics in Applied Earth Observations and Remote Sensing, 2020, 13, 4188-4199. | 4.9 | 19 |
| 96 | Fault Geometry and Slip Distribution of the 2010 Yushu Earthquakes Inferred from InSAR Measurement. Bulletin of the Seismological Society of America, 2011, 101, 1951-1958. | 2.3 | 18 |
| 97 | Synergetic Classification of Coastal Wetlands over the Yellow River Delta with GF-3 Full-Polarization SAR and Zhuhai-1 OHS Hyperspectral Remote Sensing. Remote Sensing, 2021, 13, 4444. | 4.0 | 18 |
| 98 | Interseismic slip rate of the Garze–Yushu fault belt in the Tibetan Plateau from C-band InSAR observations between 2003 and 2010. Advances in Space Research, 2011, 48, 2005-2015. | 2.6 | 17 |
| 99 | Three-dimensional (3D) morphology of Sansha Yongle Blue Hole in the South China Sea revealed by underwater remotely operated vehicle. Scientific Reports, 2018, 8, 17122. | 3.3 | 17 |
| 100 | Statistical assessment metrics for InSAR atmospheric correction: Applications to generic atmospheric correction online service for InSAR (GACOS) in Eastern China. International Journal of Applied Earth Observation and Geoinformation, 2021, 96, 102289. | 2.8 | 17 |
| 101 | Identifying barriers to sustainable apple production: A stakeholder perspective. Journal of Environmental Management, 2022, 302, 114082. | 7.8 | 17 |
| 102 | A study on the applicability of repeatâ€pass SAR interferometry for generating DEMs over several Indian test sites. International Journal of Remote Sensing, 2006, 27, 595-616. | 2.9 | 16 |
| 103 | The 2009 L'Aquila <italic>M</italic> _W 6.3 earthquake: a new technique to locate the hypocentre in the joint inversion of earthquake rupture process. Geophysical Journal International, 0, , . | 2.4 | 16 |
| 104 | A Multi-Scale Deep Neural Network for Water Detection from SAR Images in the Mountainous Areas. Remote Sensing, 2020, 12, 3205. | 4.0 | 16 |
| 105 | InSAR Time Series Analysis of L-Band Data for Understanding Tropical Peatland Degradation and Restoration. Remote Sensing, 2019, 11, 2592. | 4.0 | 15 |
| 106 | Modelling of instrument repositioning errors in discontinuous Multi-Campaign Ground-Based SAR (MC-GBSAR) deformation monitoring. ISPRS Journal of Photogrammetry and Remote Sensing, 2019, 157, 26-40. | 11.1 | 15 |
| 107 | Probing Coulomb stress triggering effects for a Mw > 6.0 earthquake sequence from 1997 to 2014 along the periphery of the Bayan Har block on the Tibetan Plateau. Tectonophysics, 2017, 694, 249-267. | 2.2 | 14 |
| 108 | A New Baseline Linear Combination Algorithm for Generating Urban Digital Elevation Models With Multitemporal InSAR Observations. IEEE Transactions on Geoscience and Remote Sensing, 2020, 58, 1120-1133. | 6.3 | 14 |

| # | Article | IF | CITATIONS |
|-----|--|-----|-----------|
| 109 | Quantifying Ground Subsidence Associated with Aquifer Overexploitation Using Space-Borne Radar Interferometry in Kabul, Afghanistan. Remote Sensing, 2020, 12, 2461. | 4.0 | 14 |
| 110 | Effects of Agricultural Cooperative Society on Farmers' Technical Efficiency: Evidence from Stochastic Frontier Analysis. Sustainability, 2020, 12, 8194. | 3.2 | 14 |
| 111 | Diagnosing Subsidence Geohazard at Beijing Capital International Airport, from High-Resolution SAR Interferometry. Sustainability, 2020, 12, 2269. | 3.2 | 14 |
| 112 | Retrieving Three-Dimensional Large Surface Displacements in Coal Mining Areas by Combining SAR Pixel Offset Measurements with an Improved Mining Subsidence Model. Remote Sensing, 2021, 13, 2541. | 4.0 | 14 |
| 113 | Mapping Tidal Flats of the Bohai and Yellow Seas Using Time Series Sentinel-2 Images and Google Earth Engine. Remote Sensing, 2022, 14, 1789. | 4.0 | 14 |
| 114 | Analysis of Present Tectonic Stress and Regional Ground Fissure Formation Mechanism of the Weihe Basin. Survey Review, 2011, 43, 382-389. | 1.2 | 13 |
| 115 | Rupture history of the 2010 Ms 7.1 Yushu earthquake by joint inversion of teleseismic data and InSAR measurements. Tectonophysics, 2013, 584, 129-137. | 2.2 | 13 |
| 116 | A new quality validation of global digital elevation models freely available in China. Survey Review, 2016, 48, 409-420. | 1.2 | 13 |
| 117 | The 2018 <i>M</i> _{<i>w</i>} 7.5 Papua New Guinea Earthquake: A Possible Complex Multiple Faults Failure Event With Deepâ€Seated Reverse Faulting. Earth and Space Science, 2020, 7, e2019EA000966. | 2.6 | 13 |
| 118 | Landslide geometry and activity in Villa de la Independencia (Bolivia) revealed by InSAR and seismic noise measurements. Landslides, 2021, 18, 2721-2737. | 5.4 | 13 |
| 119 | A proposed framework for accelerating technology trajectories in agriculture: a case study in China. Frontiers of Agricultural Science and Engineering, 2018, . | 1.4 | 13 |
| 120 | TOWARDS INSAR EVERYWHERE, ALL THE TIME, WITH SENTINEL-1. International Archives of the Photogrammetry, Remote Sensing and Spatial Information Sciences - ISPRS Archives, 0, XLI-B4, 763-766. | 0.2 | 13 |
| 121 | Time-Varying Surface Deformation Retrieval and Prediction in Closed Mines through Integration of SBAS InSAR Measurements and LSTM Algorithm. Remote Sensing, 2022, 14, 788. | 4.0 | 13 |
| 122 | MERIS Atmospheric Water Vapor Correction Model for Wide Swath Interferometric Synthetic Aperture Radar. IEEE Geoscience and Remote Sensing Letters, 2012, 9, 257-261. | 3.1 | 12 |
| 123 | Super-Resolved Multiple Scatterers Detection in SAR Tomography Based on Compressive Sensing Generalized Likelihood Ratio Test (CS-GLRT). Remote Sensing, 2019, 11, 1930. | 4.0 | 12 |
| 124 | Source parameters of the 2017 <i>M</i> w 6.2 Yukon earthquake doublet inferred from coseismic GPS and ALOS-2 deformation measurements. Geophysical Journal International, 2019, 216, 1517-1528. | 2.4 | 12 |
| 125 | Ocean Tide Loading Effects on InSAR Observations Over Wide Regions. Geophysical Research Letters, 2020, 47, e2020GL088184. | 4.0 | 12 |
| 126 | Geospatial Contextual Attention Mechanism for Automatic and Fast Airport Detection in SAR Imagery. IEEE Access, 2020, 8, 173627-173640. | 4.2 | 12 |

| # | Article | IF | CITATIONS |
|-----|---|-----|-----------|
| 127 | Time-Dependent Afterslip of the 2009 Mw 6.3 Dachaidan Earthquake (China) and Viscosity beneath the Qaidam Basin Inferred from Postseismic Deformation Observations. Remote Sensing, 2016, 8, 649. | 4.0 | 11 |
| 128 | Integration of Range Split Spectrum Interferometry and conventional InSAR to monitor large gradient surface displacements. International Journal of Applied Earth Observation and Geoinformation, 2019, 74, 130-137. | 2.8 | 9 |
| 129 | Employing deep learning for automatic river bridge detection from SAR images based on Adaptively effective feature fusion. International Journal of Applied Earth Observation and Geoinformation, 2021, 102, 102425. | 2.8 | 9 |
| 130 | A comparative review of the state and advancement of Site-Specific Crop Management in the UK and China. Frontiers of Agricultural Science and Engineering, 2019, 6, 116. | 1.4 | 9 |
| 131 | General Survey of Large-scale Land Subsidence by GACOS-Corrected InSAR Stacking: Case Study in North China Plain. Proceedings of the International Association of Hydrological Sciences, 0, 382, 213-218. | 1.0 | 9 |
| 132 | GPS automatic monitoring system for outside deformation of Geheyan Dam on the Qingjiang River. Geo-Spatial Information Science, 2000, 3, 58-64. | 5.3 | 8 |
| 133 | A New Nonlocal Method for Ground-Based Synthetic Aperture Radar Deformation Monitoring. IEEE Journal of Selected Topics in Applied Earth Observations and Remote Sensing, 2018, 11, 3769-3781. | 4.9 | 8 |
| 134 | A New Processing Chain for Real-Time Ground-Based SAR (RT-GBSAR) Deformation Monitoring. Remote Sensing, 2019, 11, 2437. | 4.0 | 8 |
| 135 | Coseismic and postseismic deformation of the 2016 Mw 6.0 Petermann ranges earthquake from satellite radar observations. Advances in Space Research, 2022, 69, 376-385. | 2.6 | 8 |
| 136 | Surface Deformation of Expansive Soil at Ankang Airport, China, Revealed by InSAR Observations. Remote Sensing, 2022, 14, 2217. | 4.0 | 8 |
| 137 | State-of-the-art in studies of glacial isostatic adjustment for the British Isles: a literature review. Earth and Environmental Science Transactions of the Royal Society of Edinburgh, 2015, 106, 145-170. | 0.3 | 7 |
| 138 | New Approaches to Processing Ground-based SAR (GBSAR) Data for Deformation Monitoring. Remote Sensing, 2018, 10, 1936. | 4.0 | 7 |
| 139 | Reconstruction and Evaluation of DEMs From Bistatic Tandem-X SAR in Mountainous and Coastal Areas of China. IEEE Journal of Selected Topics in Applied Earth Observations and Remote Sensing, 2021, 14, 5152-5170. | 4.9 | 7 |
| 140 | Wide Sliding Window and Subsampling Network for Hyperspectral Image Classification. Remote Sensing, 2021, 13, 1290. | 4.0 | 7 |
| 141 | Dynamic Wide and Deep Neural Network for Hyperspectral Image Classification. Remote Sensing, 2021, 13, 2575. | 4.0 | 7 |
| 142 | Geospatial Transformer Is What You Need for Aircraft Detection in SAR Imagery. IEEE Transactions on Geoscience and Remote Sensing, 2022, 60, 1-15. | 6.3 | 7 |
| 143 | A New Coherence Detection Method for Mapping Inland Water Bodies Using CYGNSS Data. Remote Sensing, 2022, 14, 3195. | 4.0 | 7 |
| 144 | Validating Accuracy of Rayleigh-Wave Dispersion Extracted from Ambient Seismic Noise Via Comparison with Data from a Ground-Truth Earthquake. Bulletin of the Seismological Society of America, 2014, 104, 2133-2141. | 2.3 | 6 |

| # | Article | IF | CITATIONS |
|-----|--|------------------|--------------|
| 145 | A Flexible, Generic Photogrammetric Approach to Zoom Lens Calibration. Remote Sensing, 2017, 9, 244. | 4.0 | 6 |
| 146 | Lake Level Change From Satellite Altimetry Over Seasonally Ice-Covered Lakes in the Mackenzie River Basin. IEEE Transactions on Geoscience and Remote Sensing, 2021, 59, 8143-8152. | 6.3 | 6 |
| 147 | Spatiotemporal Change Detection of Coastal Wetlands Using Multi-Band SAR Coherence and Synergetic Classification. Remote Sensing, 2022, 14, 2610. | 4.0 | 6 |
| 148 | A Combined Quantitative Evaluation Model for the Capability of Hyperspectral Imagery for Mineral Mapping. Sensors, 2019, 19, 328. | 3.8 | 5 |
| 149 | Coseismic Slip Distribution of the 2019 Mw 7.5 New Ireland Earthquake from the Integration of Multiple Remote Sensing Techniques. Remote Sensing, 2019, 11, 2767. | 4.0 | 5 |
| 150 | Simulating the Response of the Surface Urban Heat Environment to Land Use and Land Cover Changes: A Case Study of Wuhan, China. Remote Sensing, 2021, 13, 4495. | 4.0 | 5 |
| 151 | Monitoring peat subsidence and carbon emission in Indonesia peatlands using InSAR time series. , 2016, , \cdot | | 4 |
| 152 | Iterative-SGLRT for Multiple-Scatterer Detection in SAR Tomography. IEEE Geoscience and Remote Sensing Letters, 2021, 18, 122-126. | 3.1 | 4 |
| 153 | Landslide Susceptibility Mapping Using GIS-based Vector Grid File (VGF) Validating with InSAR Techniques: Three Gorges, Yangtze River (China). AIMS Geosciences, 2017, 3, 116-141. | 1.0 | 4 |
| 154 | ä,€ç§åŸºªºŽåਝæºé¥æ"Ÿçš"æ»'åţé˜²ç¾æŠ€æœ¯æ¡†æž¶åŠå…¶å·¥ç¨‹åº"ç"`. Diqiu Kexue - Zhongguo Dizhi Daxue Geosciences, 2022, 47, 1901. | Xuebao/Ea 0.5 | arth Science |
| 155 | Measuring mining induced subsidence with InSAR. , 0, , . | | 3 |
| 156 | Using small baseline Interferometric SAR to map nonlinear ground motion: a case study in Northern Tibet. Journal of Applied Geodesy, 2009, 3, . | 1.1 | 3 |
| 157 | Biomass estimation of oilseed rape using simulated compact polarimtric SAR imagery. , 2016, , . | | 3 |
| 158 | Use of Google Earth Engine to Generate a 20-Year 1 Km × 1 Km Monthly Air Temperature Product Over Yellow River Basin. IEEE Journal of Selected Topics in Applied Earth Observations and Remote Sensing, 2021, 14, 10079-10090. | 4.9 | 3 |
| 159 | TOWARDS INSAR EVERYWHERE, ALL THE TIME, WITH SENTINEL-1. International Archives of the Photogrammetry, Remote Sensing and Spatial Information Sciences - ISPRS Archives, 0, XLI-B4, 763-766. | 0.2 | 3 |
| 160 | Land subsidence in southwest Cyprus revealed from C-band radar interferometry. , 2014, , . | | 2 |
| 161 | New Advances on Environment Monitoring with Wireless Sensor Network. International Journal of Distributed Sensor Networks, 2016, 12, 2378070. | 2.2 | 2 |
| 162 | Joint Inversion of Geodetic Observations and Relative Weighting—The 1999 Mw 7.6 Chi-Chi Earthquake Revisited. Remote Sensing, 2020, 12, 3125. | 4.0 | 2 |

| # | Article | IF | CITATIONS |
|-----|---|------|-----------|
| 163 | Optimizing Global Navigation Satellite Systems network real-time kinematic infrastructure for homogeneous positioning performance from the perspective of tropospheric effects. Proceedings of the Royal Society A: Mathematical, Physical and Engineering Sciences, 2020, 476, 20200248. | 2.1 | 2 |
| 164 | Geodetic Constraints on Recent Subduction Earthquakes and Future Seismic Hazards in the Southwestern Coast of Mexico. Geophysical Research Letters, 2021, 48, e2021GL094192. | 4.0 | 2 |
| 165 | Phase unmixing of TerraSAR-X staring spotlight interferograms in building scale for PS height and deformation. ISPRS Journal of Photogrammetry and Remote Sensing, 2021, 180, 14-28. | 11.1 | 2 |
| 166 | POTENTIAL LANDSLIDE EARLY DETECTION NEAR WENCHUAN BY A QUALITATIVELY MULTI-BASELINE DINSAR METHOD. International Archives of the Photogrammetry, Remote Sensing and Spatial Information Sciences - ISPRS Archives, 0, XLII-3, 253-256. | 0.2 | 2 |
| 167 | Predicting Grain Protein Content in Winter Wheat Using Hyperspectral and Meteorological Factor. , 2018, , . | | 1 |
| 168 | Recognition of the coastal dune migration micro-deformation in Changli Gold Coast of China based on GB-InSAR. Marine Georesources and Geotechnology, 2021, 39, 747-755. | 2.1 | 1 |
| 169 | MERGING DIGITAL SURFACE MODELS IMPLEMENTING BAYESIAN APPROACHES. International Archives of the Photogrammetry, Remote Sensing and Spatial Information Sciences - ISPRS Archives, 0, XLI-B7, 711-718. | 0.2 | 1 |
| 170 | RESEARCH ON THE CRUSTAL DEFORMATION CHARACTERISTICS IN BEIJING USING INSAR AND GNSS TECHNOLOGY. International Archives of the Photogrammetry, Remote Sensing and Spatial Information Sciences - ISPRS Archives, 0, XLII-3, 559-564. | 0.2 | 1 |
| 171 | RADAR REMOTE SENSING APPLICATIONS IN LANDSLIDE MONITORING WITH MULTI-PLATFORM INSAR OBSERVATIONS: A CASE STUDY FROM CHINA. International Archives of the Photogrammetry, Remote Sensing and Spatial Information Sciences - ISPRS Archives, 0, XLII-2/W13, 1939-1943. | 0.2 | 1 |
| 172 | DEFORMATION MONITORING OF HIGH-LATITUDE PERMAFROST REGION OF NORTHEASTERN CHINA WITH TIME SERIES INSAR TECHNIQUE. International Archives of the Photogrammetry, Remote Sensing and Spatial Information Sciences - ISPRS Archives, 0, XLII-2/W13, 1777-1780. | 0.2 | 1 |
| 173 | Topographic insights in the Frome-Callabonna system and the elevation of a newly surveyed highstand shoreline. Transactions of the Royal Society of South Australia, 0, , 1-19. | 0.4 | 1 |
| 174 | Earthquake source parameters of the 2009MW7.8 Fiordland (New Zealand) earthquake from L-band InSAR observations. Earthquake Science, 2011, 24, 199-206. | 0.9 | 0 |
| 175 | ISBDD Model for Classification of Hyperspectral Remote Sensing Imagery. Sensors, 2018, 18, 780. | 3.8 | 0 |
| 176 | Study and Establishment of Regional Elastic Block Strain Model Based on GPS data. Lecture Notes in Electrical Engineering, 2012, , 267-275. | 0.4 | 0 |
| 177 | Estimation of winter wheat canopy nitrogen density at different growth stages based on Multi-LUT approach. , 2017, , . | | 0 |
| 178 | CHARACTERIZATION OF THE FROST HEAVE DEFORMATIONS IN HIGH LATITUDE AND DEEP SEASONALLY FROZEN SOIL OF INNER MONGOLIA WITH SENTINEL-1 INSAR OBSERVATIONS. International Archives of the Photogrammetry, Remote Sensing and Spatial Information Sciences - ISPRS Archives, 0, XLIII-B3-2020, 887-891. | 0.2 | 0 |
| 179 | Coastal Lowlands' Inundation Risk Assessment with High-resolution TanDEM-X DEM in Qingdao Coastal Plains, China. Proceedings of the International Association of Hydrological Sciences, 0, 382, 621-627. | 1.0 | 0 |
| | | | |

180 å·è—ëº≇€šå»Šé"林波段冰å·æ³¥çŸ³æµå'è,²åЍæ€æ¼"化å^†æžåŠç›'测é¢,,è┤方案. Diqiu Kexue - Zhongguo Dizhi Daxue Xue Geosciences, 2022, 47, 1969.